Progress In Electromagnetics Research C, Vol. 105, 253–269, 2020

Sparse Self-Calibration for Microwave Staring Correlated Imaging with Random Phase Errors

Bo Yuan*, Zheng Jiang, Jianlin Zhang, Yuanyue Guo, and Dongjin Wang

Abstract—Microwave Staring Correlated Imaging (MSCI) technology can obtain high-resolution images in staring imaging geometry by utilizing the temporal-spatial stochastic radiation field. In MSCI, sparse-driven approaches are commonly used to reconstruct the target images when the radiation fields are accurately calculated. However, it is challenging to compute radiation filed with high precision due to the existence of random phase errors in MSCI systems. Therefore, in this paper, a self-calibration method is proposed to handle the problem. Specifically, a two-step self-calibration framework is applied which alternately reconstructs the target image and estimates the random phase errors. In the target image reconstruction step, sparse-driven approaches are utilized, while in the random phase errors calibration step, an adaptive learning rate method is adopted. Moreover, the batch-learning strategy is utilized to reduce computation burden and obtain effective convergence performance. Numerical simulations verify the advantage of the proposed method to obtain good imaging results and improve random phase errors correction performance.

1. INTRODUCTION

Continuous observation for key areas using radar systems carried on stationary platforms has always been an important demand in military target observations, disaster monitoring, and other fields [1–3], which is called radar staring imaging (RSI) [4].

However, the conventional staring imaging radar, e.g., real aperture radar (RAR), cannot obtain satisfying high-resolution images in RSI applications [5, 6]. Recently, Microwave Staring Correlated Imaging (MSCI) technology [4, 7], also called Radar Coincidence Imaging (RCI) [8, 9], is proposed to obtain high-resolution images in the staring imaging geometry [7].

The crucial point of MSCI is to constitute the temporal-spatial stochastic radiation field (TSSRF) on the target plane, which is commonly realized by employing multi-transmitters to emit predesigned waveforms. After the interaction between the radiation field and scatterers, the scattering field is received by the receiving antenna, and the echo is sampled after the down-conversion procedure. Finally, the images are reconstructed by correlation process (CP) of the sampled echo signals and the computed TSSRF matrix. The detailed imaging process of MSCI is illustrated in Figure 1.

Waveform design is one of the main research areas in MSCI [7, 9–14]. The frequency-hopping (FH) waveforms are mostly studied given that FH waveforms are easy to generate and control by traditional radar hardwares [7, 9, 11, 12]. Therefore, a multi-transmitter MSCI system which transmits FH waveforms is considered in this paper.

The imaging results of MSCI are greatly influenced by the computational accuracy of the TSSRF matrix, which requires the precise and accurate modeling knowledge of the radar systems. Unfortunately, modeling errors always exist in MSCI systems, such as phase errors, gain errors, and synchronization

Received 1 July 2020, Accepted 3 September 2020, Scheduled 29 September 2020

* Corresponding author: Bo Yuan (yuanb@mail.ustc.edu.cn).

The authors are with the Key Laboratory of Electromagnetic Space Information, Chinese Academy of Sciences, University of Science and Technology of China, Hefei 230027, China.

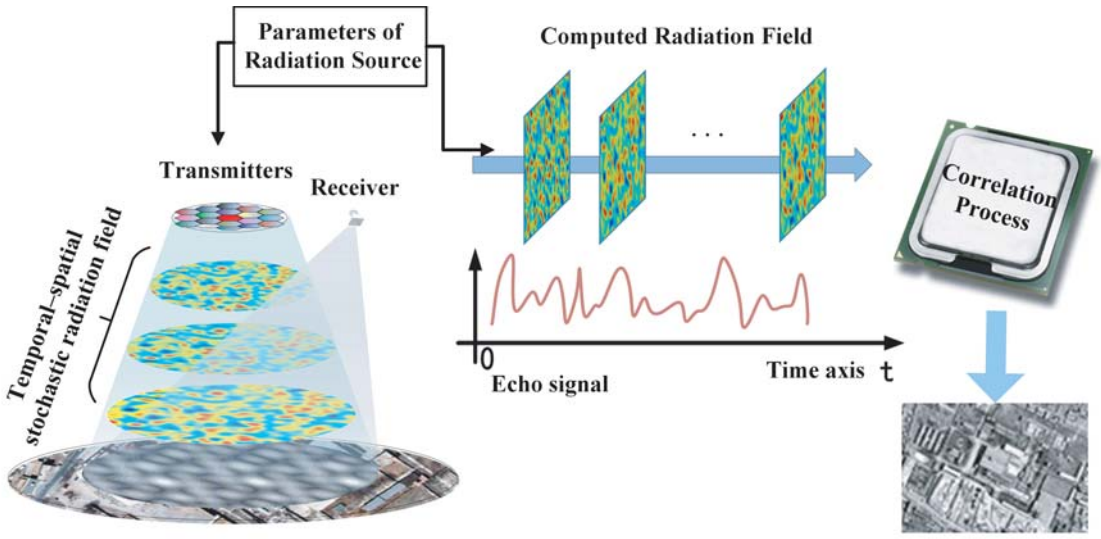

Figure 1. Imaging procedure of microwave staring correlated imaging (MSCI) [14].

errors [15–19]. Therefore, it is necessary to take consideration of modeling errors in MSCI systems in order to obtain good imaging quality. MSCI with gain-phase errors is firstly studied in [15], and a sparse calibration method is proposed by iteratively reconstructing the target images and estimating the gain-phase errors. Afterward, a sparse Bayesian learning (SBL) based alternating iteration calibration method for MSCI with channel phase errors is proposed in [20]. Besides, the array position errors in MSCI are studied in [16], and a calibration method is proposed to estimate the array position errors. For time synchronization errors, the scheme of MSCI with an additional receiver is proposed in [21] to receive the direct signals of the transmitters. Hence the time synchronization errors as well as gain-phase errors between different channels can be estimated from the directly received signals.

Random phase errors commonly exist in MSCI systems which will considerably deteriorate the imaging quality. Specially, random phase errors exist in each transmitted pulse of each channel which is different from the phase errors considered in [15, 20] considering only one phase error of each channel.

The random phase errors in MSCI are firstly taken into account in [17, 22] along with gain errors and synchronization errors, which take the co-effect of multiple modeling errors as a perturbation to the TSSRF matrix. Thus the modeling errors are compensated by alternately reconstructing the target image and estimating the perturbation matrix. However, these methods are effective only when the relative model error (RME) is relatively small. The relative model error is defined as $RME = 20\lg(\|\mathbf{E}\|_F/\|\mathbf{H}\|_F)$ in [17], where $\mathbf{E}$ is the perturbation matrix, and $\mathbf{H}$ is the true sensing matrix.

In reality, to compute the radiation filed with high precision requires accurate estimation of random phase errors. From the data acquisition perspective, the information of random phase errors between different channels is involved in the echo signals, thus it is feasible to extract the random phase information of each channel from the echoes. Once the random phase errors are estimated, the radiation matrix can be accurately recalculated. Thereupon, seeking a method which can directly correct the random phase errors is the primary objective of our study, which is also a major contribution of our work.

The difficulty of directly calibrating the random phase errors is that the number of random phase errors will explode with the increasing numbers of transmitted pulses and channels. In addition, different from phase error calibration problems in synthetic aperture radar (SAR) [23], inverse synthetic aperture radar (ISAR) [24] and multiple-input multiple-output (MIMO) radar imaging [25] that the phase errors of different pulses and different channels are not involved with each other, the random phase errors in MSCI are correlated between different channels considering that the signals of different channels are not separated in correlation process [7, 8]. The above reasons make the direct compensation of random phase errors much more difficult.

As far as we know, there are no researches that have considered to directly calibrate the random phase errors in MSCI. The self-calibration method developed in this paper will take alternately steps to reconstruct the target image and estimate the random phase errors, as the most self-calibration methods do [15, 20, 23, 25]. Since the reconstruction of the target image and the estimation of random phase errors are involved with each other, the estimation accuracy of the random phase errors will have great influence on the results of the reconstructed target image, and vice versa. So the image recovery algorithm in this paper should be elaborately designed.

Up to now, the correlation process (CP) algorithms of MSCI include the first order correlated process algorithm [7] and some linear inverse problem solving algorithms [7, 9, 11, 15, 20]. The imaging model of MSCI is an inverse electromagnetic scattering problem and conforms with sparsity recovery [7, 11]. Thus some sparse recovery algorithms are utilized to improve the imaging performance in MSCI [11, 15, 20] when the target scatterers are sparse. Nonetheless, most of the CP algorithms based on sparse recovery methods only exploit the sparsity of the target scene without considering any particular structures [7, 9, 11, 15].

In practice, targets also exhibit cluster structures in spatial domain besides the sparsity. More importantly, exploiting the inherent structure information of the target has shown great potential to improve the reconstruction performance [26–28]. Recently, an Adaptive Clustered Sparse Bayesian Learning (ACSBL) algorithm is proposed and shows satisfactory imaging results in MSCI [29]. Therefore, in target reconstruction step of the proposed method, the clustered sparse prior proposed in ACSBL is adopted [29].

To sum up, in this paper, a self-calibration imaging method for MSCI is proposed to handle the random phase error problem. A two step self-calibration framework is applied which alternately reconstructs the target image and estimates the random radiation errors. Furthermore, the batch-learning strategy is utilized to reduce computation burden and obtain effective convergence performance. As a consequence, the proposed method achieves good image results and corrects random phase errors with considerable accuracy.

The remainder of this paper is outlined as follows. The imaging model of MSCI emitting FH signals with random phase errors is established in Section 2. In Section 3, the proposed self-calibration method is given. Simulations are taken to verify the effectiveness of the proposed method in Section 4. Conclusions are drawn in Section 5.

Notations used in this paper are as follows. The vectors and matrices are denoted by bold italics letters, e.g., $\mathbf{x}$; $\mathbf{H}$; $\boldsymbol{\sigma}$, whereas the scalars are denoted by normal italics letters, e.g., η. $\mathbf{x}^T$ and $\mathbf{x}^H$ denote the transpose and conjugate transpose of $\mathbf{x}$, respectively. In addition, $\mathbf{x} \in \mathbb{C}^M$ represents a column vector of length M with complex elements. $\|\mathbf{x}\|_2$ represents l_2 norm of vector $\mathbf{x}$. Besides, x_n denotes the n-th element of t vector $\mathbf{x}$; $[\mathbf{H}]_{mn}$ denotes the n-th element of the m-th row in the matrix $\mathbf{H}$; and $\mathbf{H}_{\cdot j}$ denotes the j-th column of the matrix $\mathbf{H}$. $card(\Omega)$ represents the number of elements in the set Ω. In addition, $\odot$ represents the Hadamard product, and $det(\mathbf{X})$ represents the determinant of the square matrix $\mathbf{X}$.

2. PROBLEM FORMULATION

The imaging geometry of the MSCI system is illustrated in Figure 2. Let (x, y, z) be Cartesian coordinates, and the origin O is located at the center of the imaging area which is labeled as G. The MSCI system on a stationary platform is above the ground with the height being h and the squint angle being θ as illustrated in Figure 2.

The transmitting antenna aperture, whose center is $(0, -h\tan\theta, h)$, is labeled as D. In addition, the location vectors of the i-th transmitting antenna and the receiving antenna are denoted by $\vec{r}_i$ and $\vec{r}_o$, respectively.

The transmitted frequency-hopping (FH) signal of the i-th transmitter with random phase errors is:

$$S_i(t) = \sum_{l=1}^{L} u_{\Delta\tau}(t - lT) e^{j2\pi f_{i,l}(t-lT)+j\varphi_{il}} \tag{1}$$

where $\Delta\tau$ is the pulse width, T the pulse period, and $f_{i,l}$ the l-th hopping frequency of the i-th

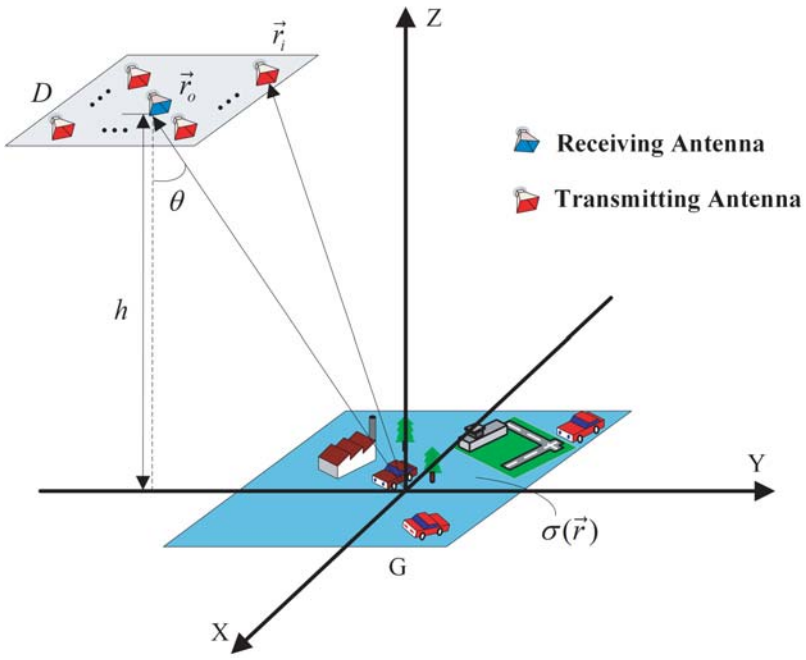

Figure 2. Imaging geometry of MSCI system.

transmitter whereas φ_{il} denotes the random phase errors.

$u_{\Delta\tau}(t)$ is

$$u_{\Delta\tau}(t) \triangleq \begin{cases} 1 & 0 < t < \Delta\tau \\ 0 & \text{otherwise} \end{cases}$$

The radiation field of the i-th transmitter thus can be expressed as:

$$E^i_{rad}(\vec{r},t) = \frac{A_i\left(\hat{\vec{R}}_{i,\vec{r}}\right)}{4\pi|\vec{r}-\vec{r}_i|}\sum_{l=1}^{L} u_{\Delta\tau}\left(t - lT - \frac{|\vec{r}-\vec{r}_i|}{c}\right) e^{j2\pi f_{i,l}\left(t-lT-\frac{|\vec{r}-\vec{r}_i|}{c}\right)+j\varphi_{il}} \tag{2}$$

where $\hat{\vec{R}}_{i,\vec{r}} = (\vec{r}-\vec{r}_i)/|\vec{r}-\vec{r}_i|$, $A_i(\hat{\vec{R}}_{i,\vec{r}})$ is the antenna pattern of the i-th antenna, and c denotes the speed of light.

Therefore, the total incident field $E_{rad}(\vec{r},t)$ at the spatial location $\vec{r}$ is the superposition of the radiation fields of all transmitters [4, 7]:

$$E_{rad}(\vec{r},t) = \sum_{i=1}^{I}\frac{A_i\left(\hat{\vec{R}}_{i,\vec{r}}\right)}{4\pi|\vec{r}-\vec{r}_i|}\sum_{l=1}^{L} u_{\Delta\tau}\left(t - lT - \frac{|\vec{r}-\vec{r}_i|}{c}\right) e^{j2\pi f_{i,l}\left(t-lT-\frac{|\vec{r}-\vec{r}_i|}{c}\right)+j\varphi_{il}} \tag{3}$$

The scattering field is received by the receiving antenna, and after the down-converting procedure, the received echo signal can be expressed in Eq. (4) [7, 8]:

$$\begin{aligned} y(t) &= \int_G \frac{A_o\left(\hat{\vec{R}}_{o,\vec{r}}\right) E_{rad}\left(\vec{r}, t-|\vec{r}-\vec{r}_o|/c\right)}{4\pi|\vec{r}-\vec{r}_o|}\sigma(\vec{r})\,d\vec{r} + n(t) \\ &= \int_G \sum_{i=1}^{I}\frac{A_i\left(\hat{\vec{R}}_{i,\vec{r}}\right)A_o\left(\hat{\vec{R}}_{o,\vec{r}}\right)}{(4\pi)^2|\vec{r}-\vec{r}_i||\vec{r}-\vec{r}_o|}\sum_{l=1}^{L} u_{\Delta\tau}(t-lT-\tau_i(\vec{r}))e^{j2\pi f_{i,l}(t-lT-\tau_i(\vec{r}))+j\varphi_{il}}\sigma(\vec{r})d\vec{r} + n(t) \end{aligned} \tag{4}$$

where G is the imaging area within the beam coverage, and $\tau_i(\vec{r}) = \frac{|\vec{r}_i-\vec{r}|+|\vec{r}_o-\vec{r}|}{c}$ is the propagation delay between the i-th transmitter and the receiver with respect to the scatterers. $\hat{\vec{R}}_{o,\vec{r}} = (\vec{r}-\vec{r}_o)|/|\vec{r}-\vec{r}_o|$

and $A_o(\hat{\vec{R}}_{o,\vec{r}})$ is the antenna pattern of the receiving antenna. Besides, $\sigma(\vec{r})$ denotes the backscattering coefficient distribution of the scatterer located at $\vec{r}$ in the imaging region, and $n(t)$ denotes the additive noise.

Define the modified radiation field $H(\vec{r},t)$ as follows:

$$H(\vec{r},t)=\sum_{i=1}^{I}H^i(\vec{r},t) \tag{5}$$

where $H^i(\vec{r},t)$ is defined as

$$H^i\left(\vec{r},t\right)=\frac{A_i\left(\hat{\vec{R}}_{i,\vec{r}}\right)A_o\left(\hat{\vec{R}}_{o,\vec{r}}\right)}{(4\pi)^2|\vec{r}-\vec{r}_i||\vec{r}-\vec{r}_o|}\sum_{l=1}^{L}u_{\Delta\tau}(t-lT-\tau_i(\vec{r})e^{j2\pi f_{i,l}(t-lT-\tau_i(\vec{r}))+j\varphi_{il}} \tag{6}$$

Thus the integral form of the imaging equation can be rewritten as:

$$y(t)=\int\limits_{G}H(\vec{r},t)\sigma(\vec{r})d\vec{r}+n(t) \tag{7}$$

Then the imaging region G is discretized into N grid cells in order to solve the imaging equation by numerical computations. Let $\vec{r}_n$ denote the location vector of the n-th grid cell center and $\sigma_n=\sigma(\vec{r}_n)$ denote the backscattering coefficient of the n-th grid cell. After sampling the echo signal at the receiver using the Analog to Digital Converter (ADC) device, the final imaging equation can be expressed as follows:

$$\mathbf{y}=\mathbf{H}\boldsymbol{\sigma}+\mathbf{n} \tag{8}$$

where $\mathbf{y}=[y(t_1),y(t_2),\ldots,y(t_M)]^T\in\mathbb{C}^M$; t_m represents the sampling time; $\boldsymbol{\sigma}=[\sigma_1,\sigma_2,\ldots,\sigma_N]^T\in\mathbb{C}^N$ is the backscattering coefficient vector; and $\mathbf{n}$ is the additive noise vector.

Equation (8) is a typical linear inverse problem. However, because of the presence of random phase errors, the matrix $\mathbf{H}$ cannot be accurately computed with the unknown parameters $\boldsymbol{\varphi}\in\mathbb{C}^{L\times I}$ with $[\boldsymbol{\varphi}]_{li}=\varphi_{il}$. So, $\mathbf{H}$ is rewritten as $\mathbf{H}(\boldsymbol{\varphi})$ to take $\boldsymbol{\varphi}$ into consideration. Then Eq. (8) can be rewritten as:

$$\mathbf{y}=\mathbf{H}(\boldsymbol{\varphi})\boldsymbol{\sigma}+\mathbf{n} \tag{9}$$

Involving the unknown random phase errors $\boldsymbol{\varphi}$, the backscattering coefficient vector $\boldsymbol{\sigma}$ could not be reconstructed directly by the conventional CP algorithms [4, 7–9, 20]. Therefore, a self-calibration imaging method, which is presented in Section 3, is proposed to solve the problem.

3. SELF-CALIBRATION IMAGING METHOD FOR MSCI WITH RANDOM PHASE ERRORS

The reconstruction of the target image $\boldsymbol{\sigma}$ and the estimation of the random phase errors in Eq. (9) can be rewritten as:

$$(\boldsymbol{\sigma},\boldsymbol{\varphi})=\arg\min_{\boldsymbol{\sigma},\boldsymbol{\varphi}}\|\mathbf{y}-\mathbf{H}(\boldsymbol{\varphi})\boldsymbol{\sigma}\|_2^2+\Xi(\boldsymbol{\sigma}) \tag{10}$$

where $\Xi(\boldsymbol{\sigma})$ is the regularizer. From Bayesian perspective, the optimization problem in Eq. (10) is equivalent to:

$$(\boldsymbol{\sigma},\boldsymbol{\varphi})=\arg\max_{\boldsymbol{\sigma},\boldsymbol{\varphi}}p(\mathbf{y}|\boldsymbol{\sigma},\boldsymbol{\varphi})+\ln p(\boldsymbol{\sigma}) \tag{11}$$

Under the additive Gaussian noise assumption, the likelihood function of the echo signal $\mathbf{y}$ can be expressed as follows:

$$p(\mathbf{y}|\boldsymbol{\sigma},\mathbf{n})=\mathcal{CN}\left(\mathbf{y}|\mathbf{H}\boldsymbol{\sigma},\eta^{-1}\mathbf{I}\right) \tag{12}$$

where the complex Gaussian distribution $\mathcal{CN}(\mathbf{x}|\boldsymbol{\mu},\boldsymbol{\Sigma})$ is defined as $\mathcal{CN}(\mathbf{x}|\boldsymbol{\mu},\boldsymbol{\Sigma})=\frac{1}{\sqrt{det(\pi\Sigma)}}\exp\{-(\mathbf{x}-\boldsymbol{\mu})^H\boldsymbol{\Sigma}^{-1}(\mathbf{x}-\boldsymbol{\mu})\}$.

In the following, the details of the proposed method are given.

3.1. Target Image Reconstruction Step

In the target image reconstruction stage, the target image is constructed utilizing the cluster sparsity prior proposed in the ACSBL algorithm [29], in which a two-layer structured hierarchical sparse Bayesian prior is utilized. The prior of the sparse target in [29] is supposed to be:

$$p\left(\boldsymbol{\sigma}|\boldsymbol{\gamma}\right) = \prod_{n=1}^{N} \mathcal{CN}\left(\sigma_n|0,\gamma_n^{-1}\right) \tag{13}$$

$$\gamma_n = \alpha_n + \rho \sum_{j\in neighbor(n)} \alpha_j \tag{14}$$

$$p(\alpha_n) = Gamma(\alpha_n|a,b) \tag{15}$$

where $neighbor(n)$ denotes the immediate neighbor set of the n-th gird cell, and a, b are hyper-parameters. The parameter ρ represents the pattern relevance between one coefficient and its immediate neighbors. $\mathcal{CN}(\sigma_n|0,\gamma_n^{-1})$ denotes a complex Gaussian distribution with the mean being 0 and the variation being γ_n^{-1} and $Gamma(a,b)$ represent the Gamma distribution, e.g., $Gamma(x|a,b) = \frac{b^a}{\Gamma(a)}x^{a-1}e^{-bx}$, where $\Gamma(a)$ is the Gamma function.

Using variational Bayesian expectation maximization (VBEM) framework, the update rules for $\boldsymbol{\sigma}$, α_n, and η can be expressed as:

$$\boldsymbol{\Sigma} = \left(\eta\mathbf{H}^H\mathbf{H} + \boldsymbol{\Lambda}\right)^{-1} \tag{16}$$

$$\boldsymbol{\sigma} = \eta\boldsymbol{\Sigma}\mathbf{H}^H\mathbf{y} \tag{17}$$

$$\alpha_n = \frac{a+1}{b+\chi_n} \tag{18}$$

$$\eta = \frac{M}{\|\mathbf{y}-\mathbf{H}\boldsymbol{\sigma}\|_2^2 + trace(\mathbf{H}^H\mathbf{H}\boldsymbol{\Sigma})} \tag{19}$$

where M is the element number of $\mathbf{y}$ and $\chi_n = \langle\sigma_n^2\rangle + \sum_{j\in neighbor(n)}\langle\sigma_j^2\rangle$ with $\langle\sigma_n^2\rangle = \sigma_n^2 + [\boldsymbol{\Sigma}]_{nn}$. Besides, $\boldsymbol{\Lambda} = diag[\gamma_1,\gamma_2,\ldots,\gamma_N]$ where γ_n is computed by Eq. (14) with the value of $\boldsymbol{\alpha}$ in the previous iteration. For detailed derivations, readers can refer to [29].

3.2. Random Phase Errors Estimation Step

For random phase error estimation step, we rewrite $\mathbf{H}$ as $\mathbf{H}(\boldsymbol{\varphi})$ to take $\boldsymbol{\varphi}$ into consideration, then the random phase error estimation problem is expressed as:

$$\boldsymbol{\varphi} = \arg\min_{\boldsymbol{\varphi}} \|\mathbf{y}-\mathbf{H}(\boldsymbol{\varphi})\boldsymbol{\sigma}\|_2^2 \tag{20}$$

Obviously, the estimation of $\boldsymbol{\varphi}$ is a nonlinear least-squares problem which is not tractable to obtain a closed-form expression. Therefore, gradient descent method is adopted to handle this problem.

The element number of $\boldsymbol{\varphi}$ is $L\times I$, where L is the number of transmitting pulses, and I is the number of transmitters. Since the element number of $\boldsymbol{\varphi}$ is very large, we sort to the AdaDelta algorithm [30] to speed up the convergence, which is a first order gradient descent method employing adaptive learning rate.

In the v-th iteration of the AdaDelta algorithm, the updating rule for $\boldsymbol{\varphi}(v)$ is

$$\begin{aligned}
\boldsymbol{\zeta}(v) &= \nabla g(\boldsymbol{\varphi}(v-1)) \\
\boldsymbol{\kappa}(v) &= \varrho\,\boldsymbol{\kappa}(v-1) + (1-\varrho)\boldsymbol{\zeta}(v)\odot\boldsymbol{\zeta}(v) \\
\boldsymbol{\nu}(v) &= \sqrt{\frac{\boldsymbol{\xi}(v-1)+\varepsilon}{\boldsymbol{\kappa}(v)+\varepsilon}}\odot\boldsymbol{\zeta}(v) \\
\boldsymbol{\varphi}(v) &= \boldsymbol{\varphi}(v-1) - \boldsymbol{\nu}(v) \\
\boldsymbol{\xi}(v) &= \varrho\boldsymbol{\xi}(v-1) + (1-\varrho)\boldsymbol{\nu}(v)\odot\boldsymbol{\nu}(v)
\end{aligned} \tag{21}$$

where $g(\boldsymbol{\varphi}) = \|\mathbf{y} - \mathbf{H}(\boldsymbol{\varphi})\boldsymbol{\sigma}\|_2^2$, $\nabla g(\boldsymbol{\varphi})$ can be computed by Eq. (A2) in Appendix A. $\boldsymbol{\kappa}(v)$ and $\boldsymbol{\xi}(v)$ are exponentially decaying average of the squared gradients and update respectively; ε is a constant added to maintain numerical stability; and ϱ is a tunable parameter to adjust the decaying rate.

3.3. Batch-Learning Strategy

The sampling time in each pulse should satisfies the condition $\tau_{\max} < |t - LT| < \tau_{\min} + \Delta t$, where $\tau_{\max}$ is $\max\{\tau_i(\vec{r}_n)|i \in [1, I], n \in [1, N]\}$, and $\tau_{\min}$ is $\min\{\tau_i(\vec{r}_n)|i \in [1, I], n \in [1, N]\}$, so that all the scatterer's echos are involved in the samples.

Besides, the imaging area is discretized into N grid cells, thus the number of parameters to be estimated is $N + L \times I$. Suppose that the number of samples of each pulse's echo is K, thus at most $K \times L$ equations can be used for target imaging and random phase errors estimation. However, the increasing number of equations will explode the computation time and increase the memory requirement. In addition, the target image reconstruction problem and random phase errors estimation problem are both non-convex problems. There is high probability that the optimal solutions fall into local minimums.

Accordingly, resorting to "batch-learning" or "streaming" methods, which only process a small fraction of data at a time, is a feasible way. For example, effectiveness approaches have been employed in the stochastic gradient descent algorithm [31] or the stochastic variational inference framework [32]. Batch-learning greatly reduces the computation burden. Furthermore, using a small fraction of data will introduce inherent noise in the gradient estimation, thus it helps the elimination of the random phase errors not captured by local minimum. Hence, batch-learning strategy is adopted in the proposed method.

Moreover, the data should be firstly split into different batches before batch-learning process. In order to update all the random phase errors $\boldsymbol{\varphi}$ in each iteration, samples in all L pulses should be included in each batch. Thus, the minimum batch shall contain at least one sample of each pulse. Namely, in each batch, one or more samples of each pulse are selected to constitute the imaging equations. As the number of iterations increases, all $L \times K$ samples are gradually adopted to constitute the imaging equations.

3.4. Summary

In summary, the Self-Calibration imaging method using Adaptive Cluster Sparse Bayesian Learning (SC-ACSBL) is shown in Algorithm 1.

The computational cost of the SC-ACSBL algorithm mainly comes from Eq. (16), and the matrix inversion in the calculation of $\boldsymbol{\Sigma}$ requires $O(N^3)$ multiplications. Therefore, the major computational complexity of the algorithm is determined by $O((N^3 + card(\Omega)^2 N) \times V_{\max})$ multiplications where $V_{\max}$ denotes the number of iterations, and Ω is the batch index set in Algorithm 1. As a result, the proposed algorithm suffers a high computational complexity and is time consuming. In order to further reduce the

Algorithm 1 SC-ACSBL

Input: $\mathbf{y}$, $\mathbf{H}$, a, b, ϵ, $V_{\max}$
Output: $\boldsymbol{\sigma}$, $\boldsymbol{\varphi}$
Initialization: Set $k = 0$ and $\boldsymbol{\alpha} = \mathbf{1}$, $\boldsymbol{\sigma}(0) = \mathbf{H}^H\mathbf{y}$

1: **for** v from 1 to $V_{\max}$ **do**
2: for echo of each pulse, random select one or more samples, and the according index constitute the index set Ω;
3: constitute the batch matrix equation: $\mathbf{y}_\Omega = \mathbf{H}_{\Omega\cdot}\boldsymbol{\sigma} + \mathbf{n}$;
4: update $\boldsymbol{\sigma}$, $\boldsymbol{\Sigma}$, $\boldsymbol{\alpha}$, η using $\mathbf{y}_\Omega$ and $\mathbf{H}_{\Omega\cdot}$ by Eqs. (17), (16), (18), and (19), respectively;
5: update $\boldsymbol{\varphi}$ using Eq. (21);
6: compute $\mathbf{H}(\boldsymbol{\varphi})$ with new $\boldsymbol{\varphi}$;
7: if $\|\hat{\boldsymbol{\sigma}}(v+1) - \hat{\boldsymbol{\sigma}}(v)\|^2 / \|\hat{\boldsymbol{\sigma}}(v)\|^2 < \epsilon$, break
8: **end for**

computation burden, we prefer to select only one sample of each pulse to constitute Ω in each iteration, e.g., $card(\Omega) = L$.

4. SIMULATIONS AND DISCUSSIONS

In this section, numerical simulations are performed to show the performance of the proposed algorithms.

Firstly, numerical experiment results of the proposed method and other existing methods are studied and compared to show the merits of our proposed algorithm. Then, the performance of the proposed method versus different random phase errors is evaluated. At the same time, the performance of the proposed method versus different signal-to-noise ratio (SNR) levels is also provided.

The imaging scenario for the simulations is shown in Figure 2. The imaging distance is set to 600 m in all the simulations. An X-band MSCI system with carrier frequency of 9.2 GHz is considered while the band of the baseband signal is 300 $\sim$ 1100 MHz with the hopping frequencies randomly chosen in the band range, and the squint angle θ is 45°. The radar consists of 24 transmitters and one receiver. $L = 2000$ frequency-hopping pulses are transmitted during the imaging procedure, thus there are $L \times I = 2000 \times 24 = 48000$ random phase errors to be calibrated. The detailed parameters of the simulations are given in Table 1. In addition, the configurations of transmitting and receiving antennas and the target image are illustrated in Figure 3.

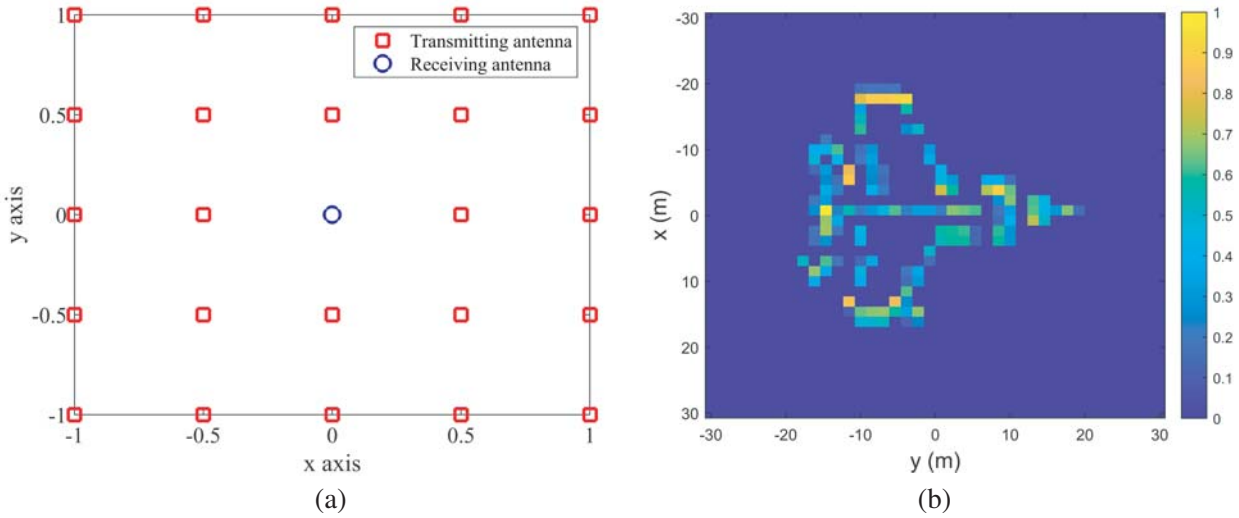

Figure 3. (a) The configuration of transmitting and receiving antennas; (b) Target image.

Besides, the hyper-parameters of a, b are all set to 1×10^{-6}. $\boldsymbol{\alpha}(0)$ is set to $\mathbf{1}$ while $\eta(0)$ is set to $100\, M/norm^2(\mathbf{y})$. In addition, ϱ in Eq. (21) is set to 0.8 and $\boldsymbol{\varphi}(0)$ set to $\mathbf{0}$.

To quantitatively describe the recovery results, normalized mean square error (NMSE) and image correlation value [26] are used as two metrics to measure the similarities to the original image. The definitions of the normalized mean-square error (NMSE) and image correlation value are given in Eqs. (22) and (23), respectively.

$$NMSE(\hat{\boldsymbol{\sigma}}) = 10 \lg \left(\|\hat{\boldsymbol{\sigma}} - \boldsymbol{\sigma}\|_2^2 / \|\boldsymbol{\sigma}\|_2^2 \right) \tag{22}$$

$$Corr\left(\hat{\boldsymbol{\sigma}}, \boldsymbol{\sigma}\right) = \left| \frac{\langle \hat{\boldsymbol{\sigma}}, \boldsymbol{\sigma} \rangle}{\|\hat{\boldsymbol{\sigma}}\|_2 \|\boldsymbol{\sigma}\|_2} \right| \tag{23}$$

where $\hat{\boldsymbol{\sigma}}$ and $\boldsymbol{\sigma}$ are estimated and true values, respectively. Commonly, a smaller NMSE and a bigger image correlation value represent better imaging performance.

Table 1. Simulation parameters.

Parameter	Value
Number of transmitters I	24
Number of receiver	1
Aperture size of Transmitting Array	$2\,\mathrm{m} \times 2\,\mathrm{m}$
Squint angle θ	45°
Size of the imaging region	$60\,\mathrm{m} \times 60\,\mathrm{m}$
Imaging Distance	600 m
Grid cell size	$1.5\,\mathrm{m} \times 1.5\,\mathrm{m}$
Carrier frequency f_0	9.2 GHz
Baseband Range	$300 \sim 1100$ MHz
Pulse number L	2000
Pulse repetition period T	10 μs
Pulse width $\Delta\tau$	500 ns

4.1. RME versus Different Random Phase Errors

In order to depict the influence of the random phase errors, two different distributions of random phase errors are evaluated. The random phase errors are supposed to follow Gaussian distributions and uniform distributions. When random phase errors follow Gaussian distributions, the standard deviation (SD) of $\boldsymbol{\varphi}$, denoted as $SD(\boldsymbol{\varphi})$, varies from 10° to 80°, whereas the random phase errors follow uniform distributions, and the range of uniform distributions varies from 10° to 360°. The RMEs versus different random phase errors are given in Figure 4. Whether the random phase errors follow Gaussian distributions or uniform distributions, it can be seen that the RME increases rapidly when the standard deviation $\boldsymbol{\varphi}$ or the range of $\boldsymbol{\varphi}$ increases. Thus it is difficult to accurately compensate the perturbation matrix.

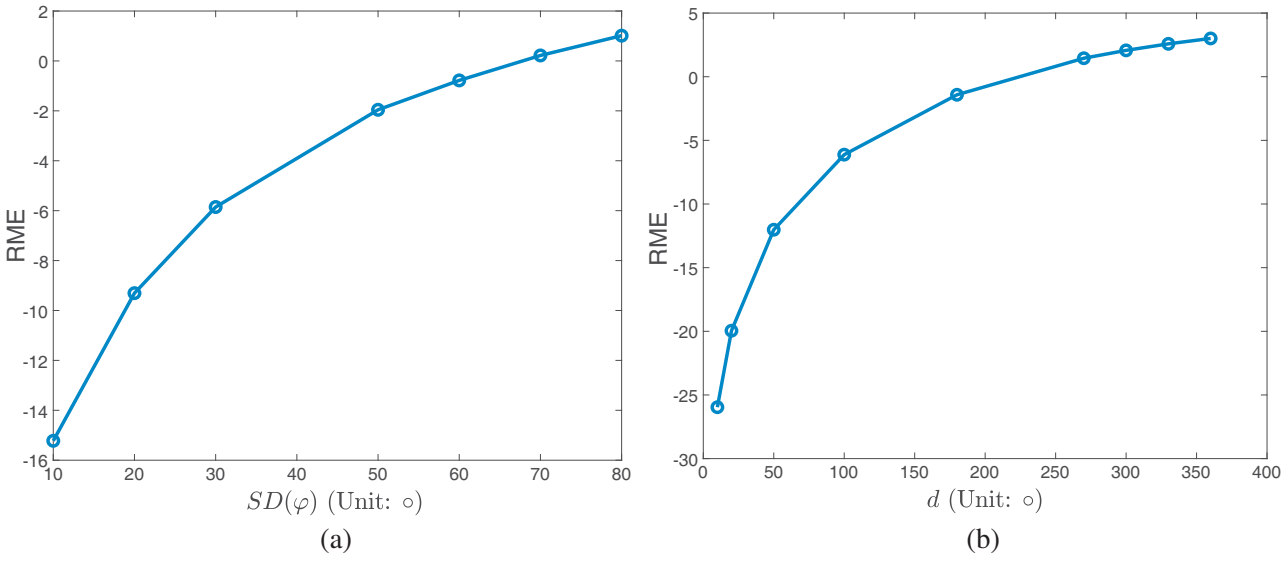

Figure 4. RME versus different random phase errors. (a) The random phase errors $\boldsymbol{\varphi}$ are supposed to follow Gaussian distributions with the standard deviation $\boldsymbol{\varphi}$, i.e., $SD(\boldsymbol{\varphi})$, varying from 10° to 80°; (b) The random phase errors $\boldsymbol{\varphi}$ are supposed to follow uniform distributions in the interval $[-\frac{d}{2}, -\frac{d}{2}]$ with d varying from 10° to 360°.

4.2. Imaging Simulations with Random Phase Errors

To verify the effectiveness of the proposed method, the following simulations are carried out. The parameters in the simulations are given in Table 1.

In one simulation, the distribution of the random phase errors is set as a Gaussian distribution with the standard deviation (SD) is 50°, while in another simulation, the distribution of the random phase errors is set as a uniform distribution with the range d being 180°.

The random phase errors have also been considered in [17, 22], which are referred as TV-TLS and R-FOUCSS, respectively. TV-TLS and R-FOUCSS methods take the effect of the modeling errors as a perturbation to the TSSRF matrix, i.e., $\mathbf{y} = (\mathbf{H} + \mathbf{E})\boldsymbol{\sigma} + \mathbf{n}$, and they prefer to compensate the perturbation matrix $\mathbf{E}$ rather than directly compensate the random phase errors. TV-TLS and R-FOUCSS methods aim to find the solutions of the following optimization problem:

$$\arg\min_{\boldsymbol{\sigma},\mathbf{E}} \|\mathbf{y} - (\mathbf{H} + \mathbf{E})\boldsymbol{\sigma}\|_2^2 + \lambda_1 \|\mathbf{E}\|_F^2 + \lambda_2 \Xi(\boldsymbol{\sigma}) \tag{24}$$

where $\Xi(\boldsymbol{\sigma}) = TV(\boldsymbol{\sigma})$ in TV-TLS, $\Xi(\boldsymbol{\sigma}) = \|\boldsymbol{\sigma}\|_p^p$ in R-FOUCSS, and $TV(\boldsymbol{\sigma})$ represents the total variation regularizer. Besides, λ_1 and λ_2 are updated during iterations in R-FOCUSS.

The imaging results of the two simulations are given in Figure 5, in which the methods applied are given in the subtitle of each subfigures. It can be seen that the target images of R-FOCUSS have many noisy points, while the TV-TLS method obtains blurred results. The outline of the target is unrecognizable in Figures 5(a), (b), (e), (f). Meanwhile, the imaging results of the ACSBL algorithm are also deteriorated, whereas the proposed SC-ACSBL algorithm achieves good imaging results with the outline of the target clearly identified. As discussed in [17, 22], the R-FOCUSS and TV-TLS methods do not directly compensate the random phase errors, and they are effective only when RME is about below −15 dB. However, in the simulations in this subsection, RME is larger than −5 dB, which means that the radiation matrix is badly perturbed. Thus it is beyond the scope of the R-FOCUSS and TV-TLS methods. On the contrary, the proposed SC-ACSBL method achieves satisfactory results by directly compensating the random phase errors.

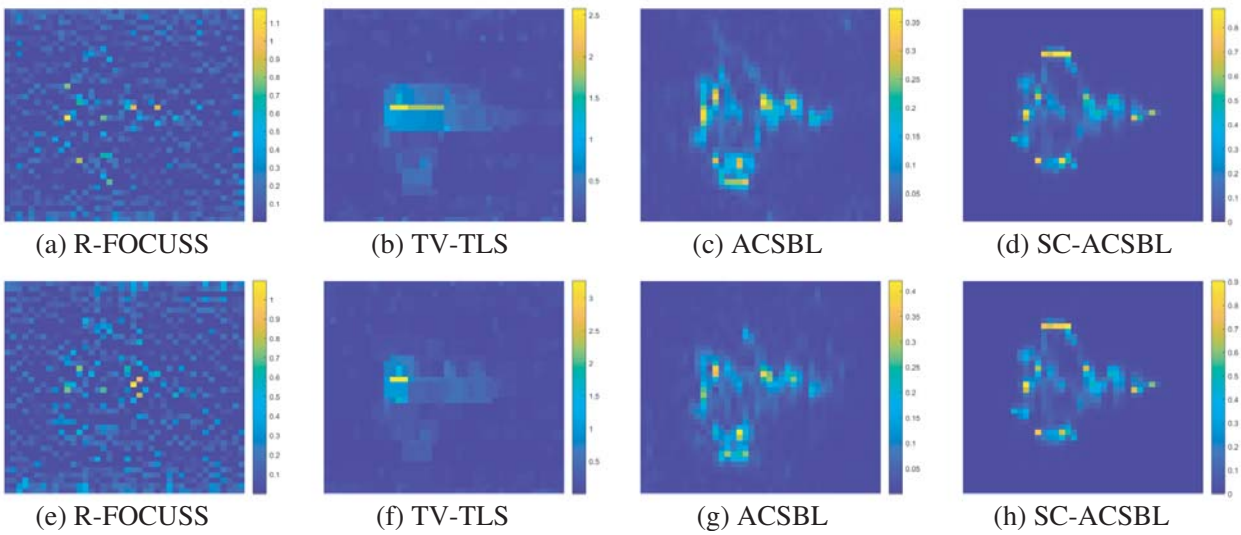

(a) R-FOCUSS (b) TV-TLS (c) ACSBL (d) SC-ACSBL

(e) R-FOCUSS (f) TV-TLS (g) ACSBL (h) SC-ACSBL

Figure 5. Imaging results. (a)–(d) The random phase errors follows a Gaussian distribution with the standard deviation (SD) is 50°; (e)–(i) The random phase errors follows a uniform distribution with d180°. (a) R-FOCUSS. (b) TV-TLS. (c) ACSBL. (d) SC-ACSBL. (e) R-FOCUSS. (f) TV-TLS. (g) ACSBL. (h) SC-ACSBL.

The histograms of the random phase errors are given in Figures 6(a), (b), and the estimation errors $\Delta\boldsymbol{\varphi} = \hat{\boldsymbol{\varphi}} - \boldsymbol{\varphi}$ are depicted in Figures 6(c), (d) with the standard deviations $SD(\Delta\boldsymbol{\varphi})$ being 7.88° and 7.92°, respectively. In addition, the estimation errors $\Delta\boldsymbol{\varphi}$ approximately follow Gauss distributions, thus about 99.7% of $\Delta\boldsymbol{\varphi}$ are within ±23.64° and ±23.75° in the two simulations.

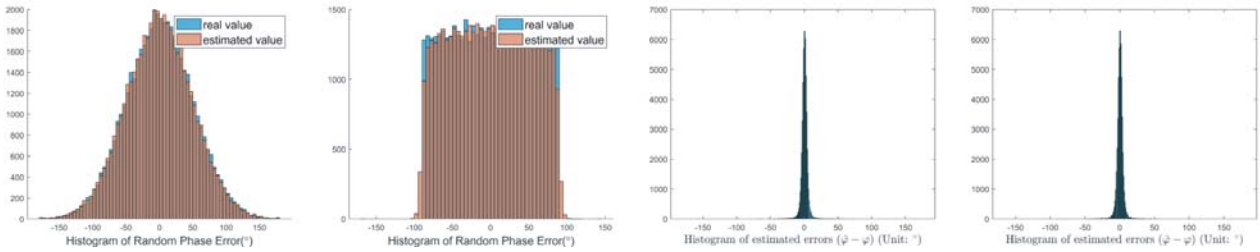

(a) (b) (c) (d)

Figure 6. Histograms of the random phase errors $\boldsymbol{\varphi}$ and the estimation errors $\Delta\boldsymbol{\varphi}$. (a) Random phase errors follows a Gaussian distribution; (b) Random phase errors follows a uniform distribution; (c) Histogram of estimated errors $\Delta\boldsymbol{\varphi}$ when random phase errors follows the Gaussian distribution; (d) Histogram of estimated errors $\Delta\boldsymbol{\varphi}$ when random phase errors follows the uniform distribution.

4.3. Simulations versus Different Random Phase Errors

In this subsection, a few simulations are conducted to verify that the proposed methods have a certain degree of tolerance for different random phase errors.

In the first group of simulations, the random phase errors follow a Gaussian distribution with $SD(\boldsymbol{\varphi})$ varying from 10° to 80°. The imaging results are illustrated in Figure 7, while in another group

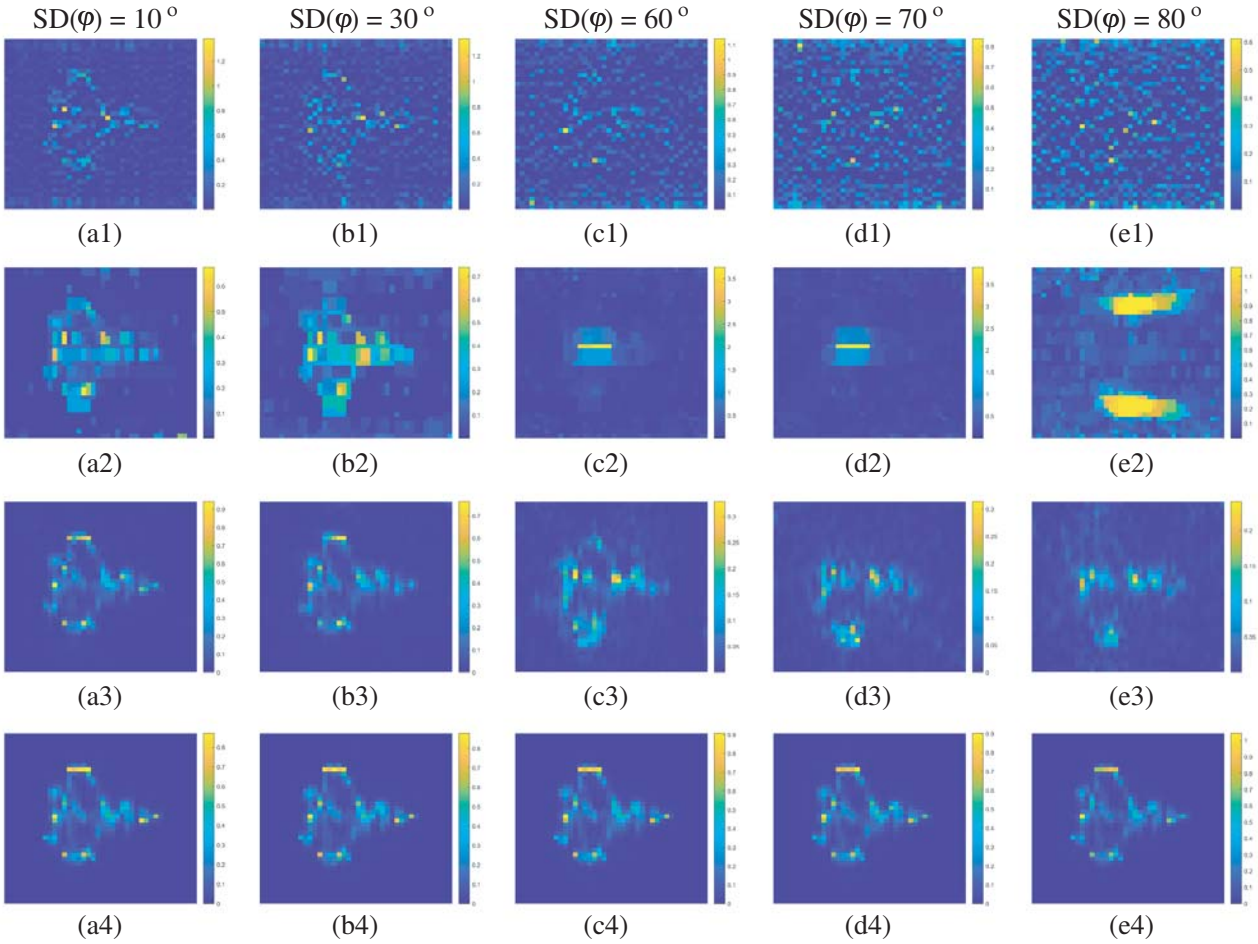

Figure 7. The imaging results when $\boldsymbol{\varphi}$ follows Gauss distributions. (a1)–(e1) R-FOCUSS; (a2)–(e2) TV-TLS; (a3)–(e3) ACSBL; (a4)–(e4) SC-ACSBL.

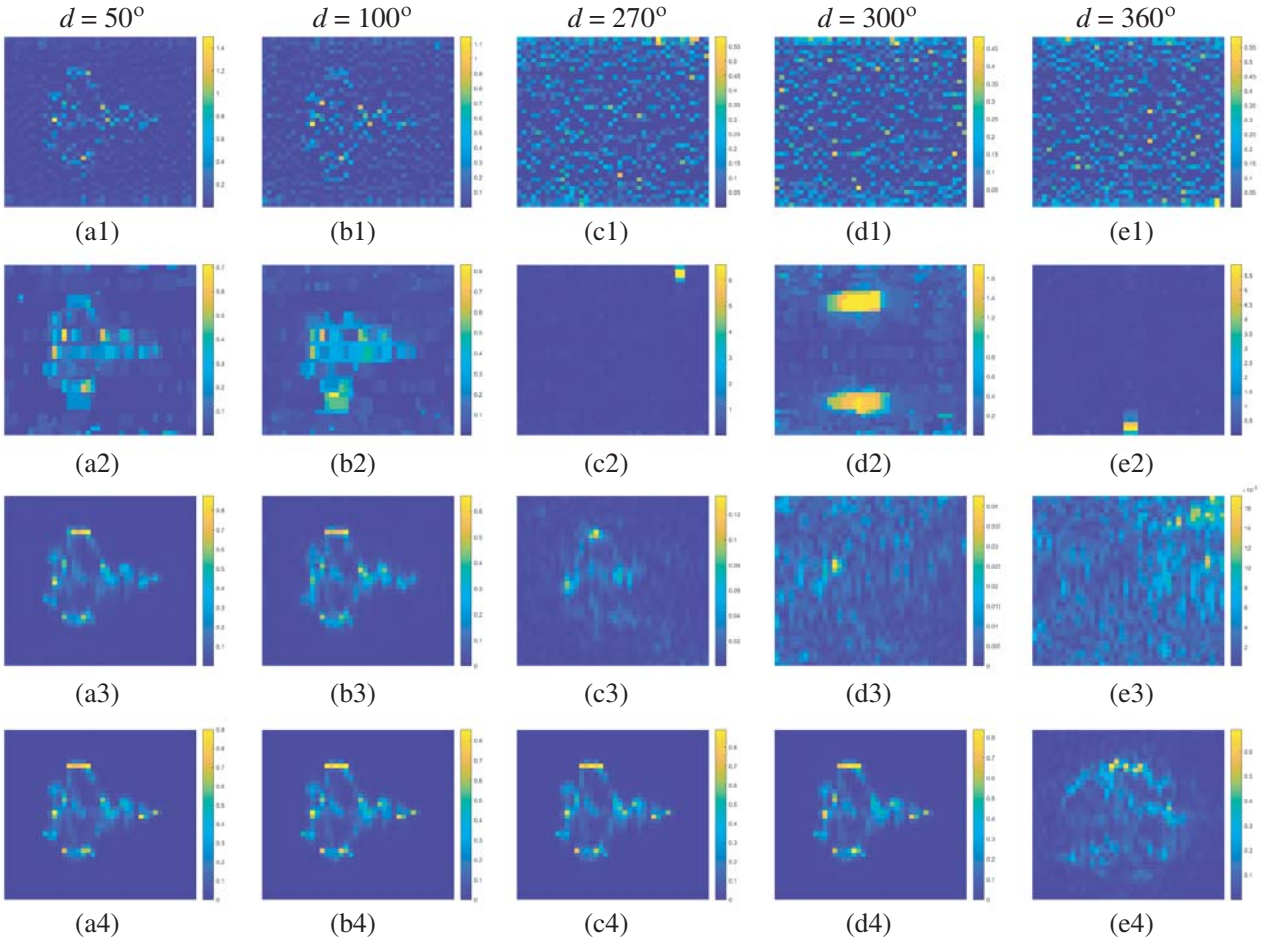

Figure 8. The imaging results when $\boldsymbol{\varphi}$ follows uniform distributions. (a1)–(e1) R-FOCUSS; (a2)–(e2) TV-TLS; (a3)–(e3) ACSBL; (a4)–(e4) SC-ACSBL.

of simulations, the random phase errors follows a uniform distribution with the ranges d varying from 50° to 360°. The imaging results are given in Figure 8.

It can be seen that when the random phase errors follow a Gaussian distribution with $SD(\boldsymbol{\varphi})$ smaller than 30°, ACSBL achieves good image quality as well as when the random phase errors follow a uniform distribution with the range d smaller than 100°. Meanwhile, the R-FOCUSS and TV-TLS methods fail to obtain target images. On the contrary, when the random phase errors follow a Gaussian distribution with $SD(\boldsymbol{\varphi})$ smaller than 80°, the proposed method achieves good image quality as well as when the random phase errors follow a uniform distribution with the range d smaller than 330°. $NMSE(\hat{\boldsymbol{\sigma}})$ and $Corr(\hat{\boldsymbol{\sigma}}, \boldsymbol{\sigma})$ of the two simulation groups are illustrated in Figure 9. It can be seen that our proposed method achieves the best $NMSE(\hat{\boldsymbol{\sigma}})$ and $Corr(\hat{\boldsymbol{\sigma}}, \boldsymbol{\sigma})$ results when the random phase errors follow Gaussian distributions and when the ranges d of uniforms distributions are within 330°, which means the best imaging performance in the simulations.

In addition, by utilizing self-calibration, the random phase errors are compensated. The real random phase errors and estimated random phase errors are depicted in Figure 10. It can be seen that the estimated random phase errors approach the true phase error distributions except when $\boldsymbol{\varphi}$ follows the Gaussian distribution with $SD(\boldsymbol{\varphi}) = 80°$ and when $\boldsymbol{\varphi}$ follows the uniform distribution with the range d being 360°. The SDs of the estimation errors $\Delta\boldsymbol{\varphi} = \hat{\boldsymbol{\varphi}} - \boldsymbol{\varphi}$ are illustrated in Figure 11. As depicted in Figure 11, $SD(\Delta\boldsymbol{\varphi})$ are all within 20° except when the random phase errors follow a uniform distribution with the range d being 360°, which means that the random phase errors are estimated within a certain degree.

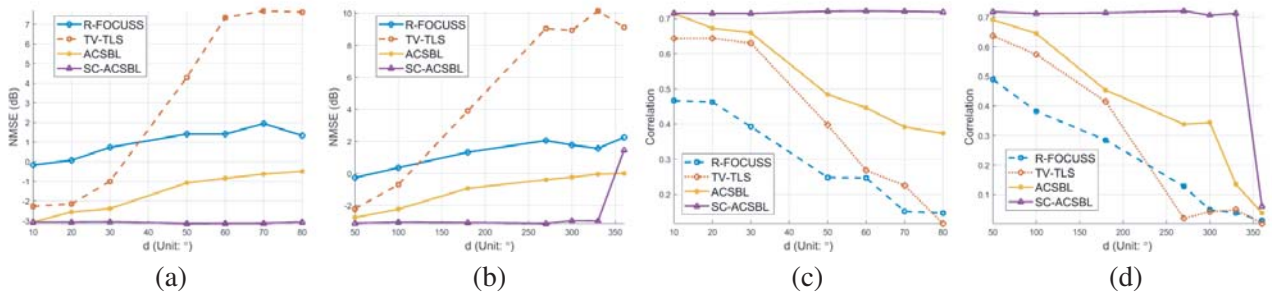

Figure 9. $NMSE(\hat{\boldsymbol{\sigma}})$ and $Corr(\hat{\boldsymbol{\sigma}}, \boldsymbol{\sigma})$. (a), (c) $\boldsymbol{\varphi}$ follows Gaussian distributions; (b), (d) $\boldsymbol{\varphi}$ follows uniform distributions. (a) $NMSE(\hat{\boldsymbol{\sigma}})$. (b) $NMSE(\hat{\boldsymbol{\sigma}})$. (c) $Corr(\hat{\boldsymbol{\sigma}}, \boldsymbol{\sigma})$. (d) $Corr(\hat{\boldsymbol{\sigma}}, \boldsymbol{\sigma})$.

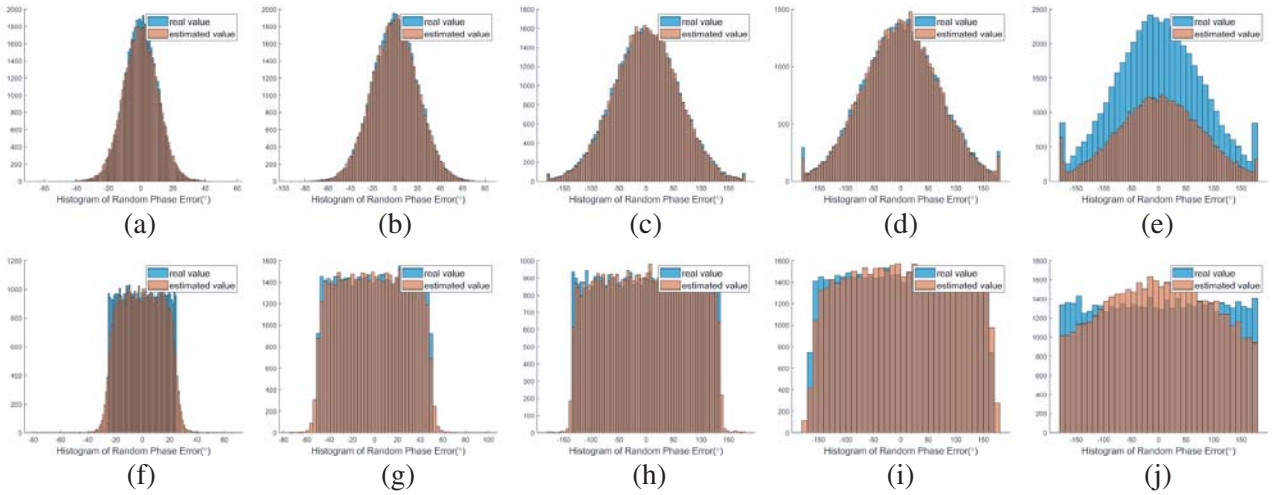

Figure 10. Histograms of the real random phase errors and the estimated random phase errors. (a)–(e) The random phase errors follows a Gauss distribution with $SD(\boldsymbol{\varphi})$ are 10°, 30°, 60°, 70°, 80° respectively; (f)–(j) The random phase errors follows a uniform distribution with range d are 50°, 100°, 270°, 330°, 360° respectively.

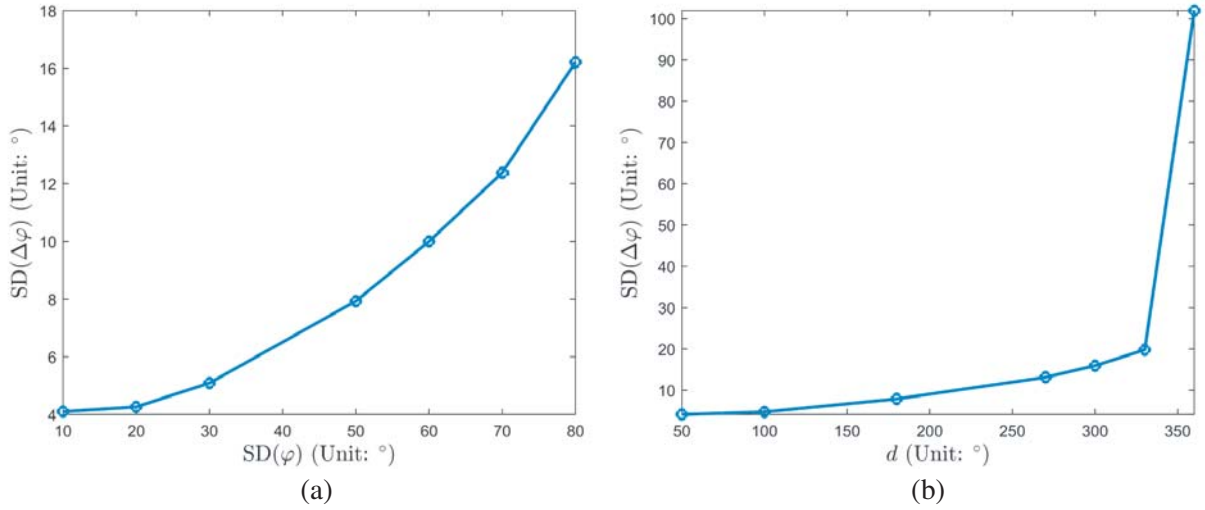

Figure 11. Standard deviation (SD) of estimated errors $\Delta\boldsymbol{\varphi}$ versus different random phase errors. (a) The random phase errors follows a Gaussian distribution with the SDs vary from 10° to 80°; (b) The random phase errors follows a uniform distribution with the ranges d vary from 50° to 360°.

4.4. Simulations versus Different SNR Levels

In order to verify the robustness to the noise of the proposed method, the following simulations are carried out in different SNRs. The echo SNRs are set from 5 dB to 25 dB with the interval of 5 dB. The random phase errors $\boldsymbol{\varphi}$ are set to follow a Gaussian distribution with $SD(\boldsymbol{\varphi}) = 70°$ and an uniform

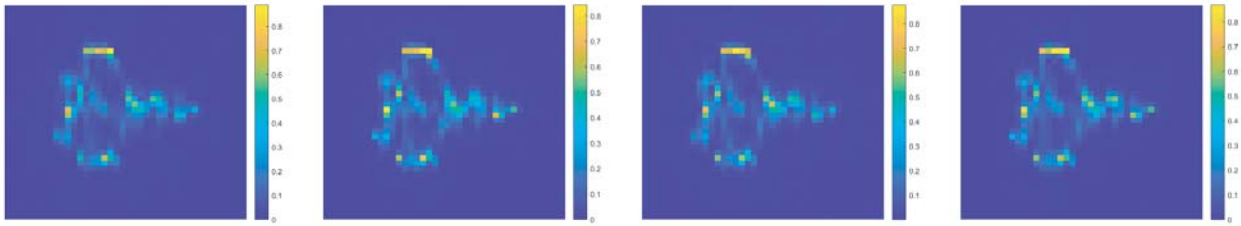

(a) *SNR* = 10 dB (b) *SNR* = 15 dB (c) *SNR* = 10 dB (d) *SNR* = 15 dB

Figure 12. Imaging results versus different SNRs. (a), (b) The random phase errors follows a Gaussian distribution with the $SD(\boldsymbol{\varphi})$ is 70°; (c), (d) The random phase errors follows a uniform distribution with the range d is 300°. (a) $SNR = 10$ dB. (b) $SNR = 15$ dB. (c) $SNR = 10$ dB. (d) $SNR = 15$ dB.

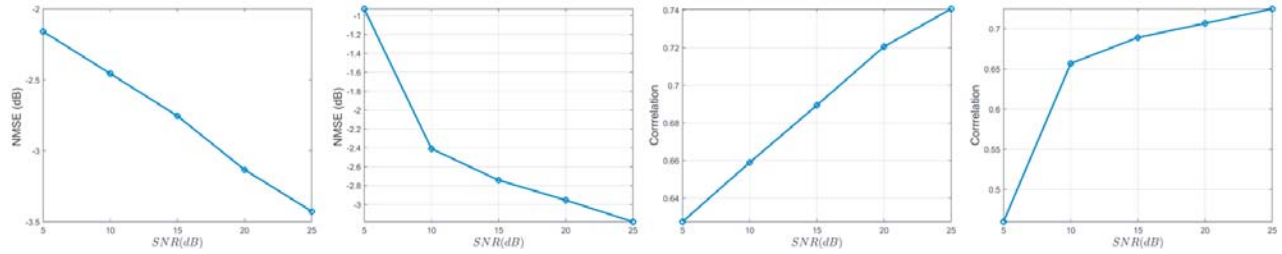

(a) (b) (c) (d)

Figure 13. $NMSE(\hat{\boldsymbol{\sigma}})$ and $Corr(\hat{\boldsymbol{\sigma}}, \boldsymbol{\sigma})$ versus different SNRs. (a), (c) The random phase errors follows a Gaussian distribution with the $SD(\boldsymbol{\varphi})$ is 70°; (b), (d) The random phase errors follows a uniform distribution with the range d is 300°. (a) $NMSE(\hat{\boldsymbol{\sigma}})$. (b) $NMSE(\hat{\boldsymbol{\sigma}})$. (c) $Corr(\hat{\boldsymbol{\sigma}}, \boldsymbol{\sigma})$. (d) $Corr(\hat{\boldsymbol{\sigma}}, \boldsymbol{\sigma})$

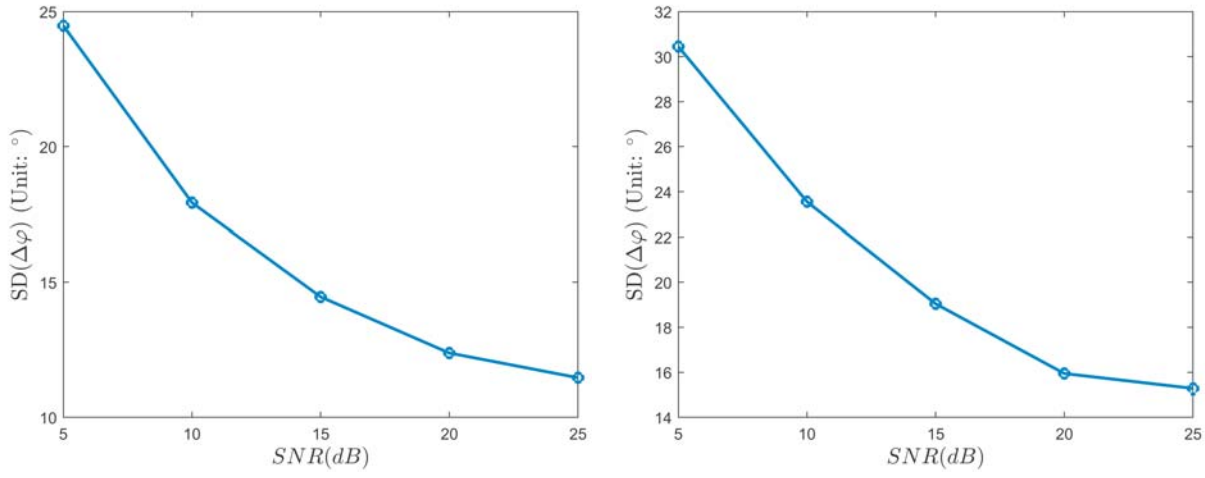

(a) (b)

Figure 14. Standard deviation (SD) of estimated errors $\Delta\boldsymbol{\varphi}$ versus different SNRs. (a) The random phase errors follows a Gaussian distribution with $SD(\boldsymbol{\varphi}) = 70°$; (b) The random phase errors follows a uniform distribution with the range d is 330°.

distribution with the range $d = 300°$. The other parameters are the same as those in Table 1, and the target scene is in Figure 3(b).

The $NMSE(\hat{\boldsymbol{\sigma}})$ and $Corr(\hat{\boldsymbol{\sigma}}, \boldsymbol{\sigma})$ versus different SNRs are given in Figure 13. Besides, the imaging results are depicted in Figure 12 when SNR is 10 dB and 15 dB. It can be seen that even when the SNR is 10 dB, the outline of the target can be clearly identified.

The $SD(\Delta\boldsymbol{\varphi})$ versus different SNRs are given in Figure 14. It can be seen that when the SNR is above 15 dB, $SD(\Delta\boldsymbol{\varphi})$ are all within 20°, which shows the robustness of SC-ACSBL to noise.

5. CONCLUSION

In this paper, random phase errors in MSCI emitting frequency-hopping waveforms are considered. In order to handle the random-phase-error problem in MSCI, a two-stage self-calibration imaging method for MSCI is proposed. As an alternating iteration algorithm, the proposed method cycles through steps of target reconstruction and random phase errors estimation, and simultaneously the batch-learning strategy is adopted to reduce the computation complexity and obtain better convergence performance. The proposed method can reconstruct the target with high imaging quality and accurately compensate the random phase errors. Simulation results illustrate the effectiveness of the proposed method in the presence of random phase errors and the robustness to noise. Meanwhile, the proposed method can estimate the random phase errors with a certain accuracy when enough echo SNR is achieved.

ACKNOWLEDGMENT

This work is supported by the National Natural Science Foundation of China under contact No. 61771446.

APPENDIX A.

In this part, the gradient $\nabla g(\boldsymbol{\varphi})$ is derived which is used in Eq. (21) to estimate the random phase errors $\boldsymbol{\varphi}$. For each batch set Ω, we rewrite $\mathbf{H}_{\Omega\cdot}$ as:

$$\mathbf{H}_{\Omega\cdot} = \sum_{i=1}^{I} \mathbf{H}^i_{\Omega\cdot} \tag{A1}$$

where the (l,n)-th element of $\mathbf{H}^i_{\Omega\cdot} \in \mathbb{C}^{L\times N}$ can be computed by $[\mathbf{H}^i_{\Omega\cdot}]_{ln} = H^i(\vec{r}_n, t_l)$. $H^i(\vec{r}, t)$ is defined in Eq. (6).

Based on the batch split strategy, the l-th sample time t_l in $\mathbf{H}^i_{\Omega\cdot}$ is within the echo of the l-th pulse, thus $\nabla g(\boldsymbol{\varphi})$ can be computed by:

$$[\nabla g(\boldsymbol{\varphi})]_{\cdot i} = -2Im\left(\left[diag(\mathbf{y}_{\Omega\cdot} - \mathbf{H}_{\boldsymbol{\Omega}\cdot}\boldsymbol{\sigma})^H\right]\left[\boldsymbol{\sigma}^H\left[\mathbf{H}^i_{\Omega\cdot}\right]^H\right]^T\right) \tag{A2}$$

where $Im()$ denotes the imaginary part, and $[\nabla g(\boldsymbol{\varphi})]_{\cdot i}$ denotes the i-th column of $\nabla g(\boldsymbol{\varphi}) \in \mathbb{C}^{L\times I}$.

REFERENCES

1. Lord, R. T and M. R. Inggs, "High resolution SAR processing using stepped-frequencies," *1997 IEEE International Geoscience and Remote Sensing, 1997, IGARSS '97, Remote Sensing — A Scientific Vision for Sustainable Development*, Vol. 1, 490–492, 1997.
2. Patel, V. M., G. R. Easley, D. M. Healy, Jr., and R. Chellappa, "Compressed synthetic aperture radar," *IEEE Journal of Selected Topics in Signal Processing*, Vol. 4, No. 2, 244–254, 2010.
3. Zhu, X. X., S. Montazeri, C. Gisinger, R. F. Hanssen, and R. Bamler, "Geodetic SAR tomography," *IEEE Transactions on Geoscience and Remote Sensing*, Vol. 54, No. 1, 18–35, 2016.

4. Ma, Y., X. He, Q. Meng, B. Liu, and D. Wang, "Microwave staring correlated imaging and resolution analysis," *Geo-Informatics in Resource Management and Sustainable Ecosystem*, 737–747, Springer, 2013.
5. Dunkel, R., R. Saddler, and A. W. Doerry, "Synthetic aperture radar for disaster monitoring," *Radar Sensor Technology XV*, 125–134, 2011.
6. Madsen, S. N. Edelstein, W. Didomenico, and L. D. Labrecque, "A geosynchronous synthetic aperture radar; for tectonic mapping, disaster management and measurements of vegetation and soil moisture," *IEEE 2001 International Geoscience and Remote Sensing Symposium, 2001, IGARSS '01*, Vol. 1, 447–449, 2002.
7. Guo, Y., X. He, and D. Wang, "A novel super-resolution imaging method based on stochastic radiation radar array," *Measurement Science and Technology*, Vol. 24, No. 7, 074013, 2013.
8. Li, D., X. Li, Y. Qin, Y. Cheng, and H. Wang, "Radar coincidence imaging: An instantaneous imaging technique with stochastic signals," *IEEE Transactions on Geoscience and Remote Sensing*, Vol. 52, No. 4, 2261–2277, 2014.
9. Cheng, Y., X. Zhou, X. Xu, Y. Qin, and H. Wang, "Radar coincidence imaging with stochastic frequency modulated array," *IEEE Journal of Selected Topics in Signal Processing*, Vol. 11, No. 2, 414–427, 2017.
10. Guo, Y., D. Wang, and C. Tian, "Research on sensing matrix characteristics in microwave staring correlated imaging based on compressed sensing," *2014 IEEE International Conference on Imaging Systems and Techniques (IST)*, 195–200, IEEE, 2014.
11. Zhou, X., H. Wang, Y. Cheng, Y. Qin, and H. Chen, "Radar coincidence imaging for off-grid target using frequency-hopping waveforms," *International Journal of Antennas & Propagation*, Vol. 2016, 1–16, 2016.
12. Zhou, X., H. Wang, Y. Cheng, Y. Qin, and H. Chen, "Waveform analysis and optimization for radar coincidence imaging with modeling error," *Mathematical Problems in Engineering*, 2017, 2017.
13. Liu, B. and D. Wang, "Orthogonal radiation field construction for microwave staring correlated imaging," *Progress In Electromagnetics Research M*, Vol. 57, 139–149, 2017.
14. Yuan, B., Y. Guo, W. Chen, and D. Wang, "A novel microwave staring correlated radar imaging method based on bi-static radar system," *Sensors*, Vol. 19, No. 4, 879, Feb. 2019.
15. Zhou, X., H. Wang, Y. Cheng, and Y. Qin, "Sparse auto-calibration for radar coincidence imaging with gain-phase errors," *Sensors*, Vol. 15, No. 11, 27611–27624, 2015.
16. Xu, X., X. Zhou, Y. Cheng, and Y. Qin, "Radar coincidence imaging with array position error," *2015 IEEE International Conference on Signal Processing, Communications and Computing (ICSPCC)*, Ningbo, China, 2015.
17. Cao, K., X. Zhou, Y. Cheng, and Y. Qin, "Improved focal underdetermined system solver method for radar coincidence imaging with model mismatch," *Journal of Electronic Imaging*, Vol. 26, No. 3, 033001, 2017.
18. Cao, K., X. Zhou, Y. Cheng, B. Fan, and Y. Qin, "Total variation-based method for radar coincidence imaging with model mismatch for extended target," *Journal of Electronic Imaging*, Vol. 26, No. 6, 063007, 2017.
19. Zhang, F., X. Liu, X. Zhou, X. Wang, and W. Liu, "Autofocus technique for radar coincidence imaging with model error via iterative maximum a posteriori," *The Journal of Engineering*, Vol. 2019, No. 19, 5837–5840, 2019.
20. Zhou, X., H. Wang, Y. Cheng, and Y. Qin, "Radar coincidence imaging with phase error using bayesian hierarchical prior modeling," *Journal of Electronic Imaging*, Vol. 25, No. 1, 013018, 2016.
21. Tian, C., B. Yuan, and D. Wang, "Calibration of gain-phase and synchronization errors for microwave staring correlated imaging with frequency-hopping waveforms," *2018 IEEE Radar Conference (RadarConf18)*, 1328–1333, 2018.
22. Cao, K., X. Zhou, Y. Cheng, Y. Qin, and K. Liu, "A method for radar coincidence imaging with model errors," *2017 International Workshop on Electromagnetics: Applications and Student Innovation Competition*, 144–146, 2017.

23. Onhon, N. and M. Cetin, "A sparsity-driven approach for joint sar imaging and phase error correction," *IEEE Transactions on Image Processing*, Vol. 21, No. 4, 2075–2088, 2012.
24. Zhao, L., L. Wang, G. Bi, and L. Yang, "An autofocus technique for high-resolution inverse synthetic aperture radar imagery," *IEEE Transactions on Geoscience and Remote Sensing*, Vol. 52, No. 10, 6392–6403, 2014.
25. Ding, L. and W. Chen, "MIMO radar sparse imaging with phase mismatch," *IEEE Geoscience and Remote Sensing Letters*, Vol. 12, No. 4, 816–820, 2015.
26. Wang, L., L. Zhao, G. Bi, C. Wan, and L. Yang, "Enhanced ISAR imaging by exploiting the continuity of the target scene," *IEEE Transactions on Geoscience and Remote Sensing*, Vol. 52, No. 9, 5736–5750, 2014.
27. Wu, Q., Y. D. Zhang, M. G. Amin, and B. Himed, "Multi-task bayesian compressive sensing exploiting intra-task dependency," *IEEE Signal Processing Letters*, Vol. 22, No. 4, 430–434, 2015.
28. Wan, C., "Sparse representation-based isar imaging using markov random fields," *IEEE Journal of Selected Topics in Applied Earth Observations and Remote Sensing*, Vol. 8, No. 8, 1–13, 2014.
29. Wang, H., Y. Qin, Y. Cheng, and X. Zhou, "Radar coincidence imaging by exploiting the continuity of extended target," *IET Radar Sonar & Navigation*, Vol. 11, No. 1, 60–69, 2017.
30. Zeiler, M. D., "Adadelta: An adaptive learning rate method," *Computer Science*, 2012.
31. Bottou, L., "Large-scale machine learning with stochastic gradient descent," *Proceedings of COMPSTAT'2010*, 177–186, Springer, 2010.
32. Hoffman, M. D., D. M. Blei, C. Wang, and J. Paisley, "Stochastic variational inference," *The Journal of Machine Learning Research*, Vol. 14, No. 1, 1303–1347, 2013.